Article

Photocatalytic Reduction of CO_2 into CO with Cyclometalated Pt(II) Complexes of N^C^N Pincer Dipyridylbenzene Ligands: A DFT Study

Antonia Sarantou and Athanassios Tsipis *

Laboratory of Inorganic Chemistry, Department of Chemistry, University of Ioannina, 45110 Ioannina, Greece; a.sarantou@uoi.gr
* Correspondence: attsipis@uoi.gr

Abstract: In this work, density functional theory (DFT) calculations were employed to study the photocatalytic reduction of CO_2 into CO using a series of Pt(II) square planar complexes with the general formula [Pt(5-R-dpb)Cl] (dpb = 1,3-di(2-pyridyl)benzene anion, R = H, *N,N*-dimethylaniline,T thiophene, diazaborinine). The CO_2-into-CO conversion process is thought to proceed via two main steps, namely the photocatalytic/reduction step and the main catalytic step. The simulated absorption spectra exhibit strong bands in the range 280–460 nm of the UV-Vis region. Reductive quenching of the T_1 state of the complexes under study is expected to be favorable since the calculated excited state redox potentials for the reaction with sacrificial electron donors are highly positive. The redox potentials reveal that the reductive quenching of the T_1 state, important to the overall process, could be modulated by suitable changes in the N^C^N pincer ligands. The CO_2 fixation and activation by the three coordinated Pt(II) catalytically active species are predicted to be favorable, with the Pt–CO_2 bond dissociation energies D_0 in the range of -36.9–-10.3 kcal/mol. The nature of the Pt–CO_2 bond of the Pt(II) square planar intermediates is complex, with covalent, hyperconjugative and H-bonding interactions prevailing over the repulsive electrostatic interactions. The main catalytic cycle is estimated to be a favorable exergonic process.

Keywords: photocatalytic CO_2 reduction; DFT/TDDFT; Pt(II) pincer complexes; T_1 excited state electrochemistry; CO_2 fixation/activation by Pt

1. Introduction

The problem of global overheating dates back long before the industrial revolution. The excessive use of fossil fuels and the massive release of greenhouse gases into the atmosphere have turned the term "global warming" into an uncomfortable reality of modern life. CO_2, although not a primary greenhouse gas, nevertheless has a significant contribution to global warming. In 2012, global CO_2 emissions, which come mainly from the burning of fossil fuels, reached a total of 34.5 billion tons [1].

The steadily increasing concentration of CO_2 in the atmosphere is now a real problem. The CO_2 emissions from the massive consumption of fossil fuels are largely responsible for global climate change: an increase in the concentration of CO_2 in the atmosphere causes global warming, as well as ocean acidification from the uptake of atmospheric CO_2 [2].

Man's growing needs for energy lead to the ominous conclusion that CO_2 emissions will not remain stagnant but will increase even more. This results in the scientific community focusing on how the abundance of CO_2 will be used to produce materials of commercial interest. Only 1‰ of the total abundance of CO_2 is currently used for chemical synthesis, which is mainly due to its chemical inertness (it is highly oxidized in nature) but also to the fact that capturing and storing CO_2 is an expensive process [3].

Many studies have focused on how to deal with the problem of the continuous increase in atmospheric CO_2 while, at the same time, there are ongoing efforts and studies not only

to capture CO_2 but also to catalytically convert it into "fine chemicals", as well as CO, CH_3OH and HCOOH [3]. A recent study by Audisio et al. demonstrated that CO, produced via a very fast photocatalytic CO_2-into-CO conversion (<10 min), could be valorized to produce radiopharmaceuticals [4].

Among various strategies to achieve this goal, the greatest and most attractive challenge is the efficient conversion of CO_2 into useful compounds using sunlight as an energy source [5]. Studies on this issue have shown the photochemical and electrochemical reduction of CO_2 into CO, into CH_3OH and also into HCOOH, using transition metal electrodes, metal complexes, semiconductors, as well as some organic molecules [6–9].

Much of the research has focused on how to sequester CO_2 from coal plant emissions, which account for 76% of all global emissions [10]. Recent advances in catalyst design combined with the reduced cost of clean energy has made the use of CO_2 more attractive as a feedstock for chemical production. Particular interest has gathered in the conversion of CO_2 into CO as a step in the petrochemical production process [11].

Mainly, there are two approaches to CO_2 reduction, namely either via heterogeneous or homogeneous catalysis. Both approaches can be achieved either electrocatalytically or photocatalytically. Heterogeneous electrocatalytic CO_2 reduction is carried out using electrolysis with the aid, for example, of nanostructured materials [12], while heterogeneous photocatalytic CO_2 reduction mainly utilizes various types of semiconductors as photocatalysts [13]. On the other hand, homogeneous electrochemical/photochemical CO_2 reduction is mainly based on transition metal complexes [14]. So far, coordination complexes of numerous metals have been studied as catalysts, such as the first row Mn, Fe, Co, Ni and Cu, also the second row Ru, Rh, Pd, as well as the third row W, Re, Os, Ir [14].

Since 1970, a great number of works have appeared in the literature concerning electrochemical/photochemical CO_2 reduction using aza macrocyclic and polypyridine complexes [15]. Along these lines, complexes of the earth-abundant Fe, Co and Ni transition metals with porphyrin-like ligands have attracted much interest. Thus, for example, a porphyrin-like aminopyridyl macrocyclic Co complex was found to be highly selective (98%) for CO production [16,17]. Fe tetraphenyl porphyrins have been demonstrated to be very active for the conversion of CO_2 into CO [15]. Water-soluble Fe-porphyrins showed very high activity (close to 100%) for CO production from CO_2 during electrolysis under low overpotential [18]. Phthalocyanine complexes of another earth-abundant, first-row Group VIII metal, namely Ni, were shown to very efficient for CO production, with nearly 100%, just like similar Co complexes [19]. In addition, other aza macrocyclic and polypyridine complexes have shown great potential for CO_2 conversion. Lioret-Fillol et al., in a combined experimental/theoretical work, studied extensively the mechanism of CO_2 reduction using a very promising Co aminopyridine catalyst [20]. Iron and cobalt quaterpyridine complexes proved to be highly efficient and selective for photocatalytic CO_2 reduction [21]. Complexes of Ni and Co with the aza-crown ether cyclam ligand have been extensively studied for CO_2 conversion [15]. In a pioneering study, Tinnemans et al. employed Ni as well as Co cyclams to photocatalytically reduce CO_2 [22]. Since then, numerous studies on cyclam complexes have appeared. A simple Ni cyclam complex exhibited high catalytic activity for CO_2 reduction, and this was attributed to the complex stabilization due to the presence of a cyclam ring, as well as to an acidic N-H proton [23–25]. Finally, studies have demonstrated that complexes of Mn with electron-rich ligands such as bipyridine are effective in CO_2 reduction [26].

Up to now, Ru and Re complexes have received the major focus and are the most widely studied. Probably, the interest in these complexes stems from the inspiring seminal works of Lehn et al. [27–29], who studied electro/photocatalytic CO_2 reduction using Re(I) and Ru(II) complexes. Since then, many other Re(I) and Ru(II) complexes have been studied for electro/photocatalytic CO_2 reduction [2,30,31].

The reduction of CO_2 into either CO or HCOOH proceeds via the following chemical equations:

$$CO_2 + 2e^- + 2H^+ \rightarrow CO + H_2O \tag{1}$$

$$CO_2 + 2e^- + 2H^+ \rightarrow HCOOH \qquad (2)$$
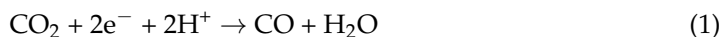
The reduction potentials of the above $2e^-/2H^+$ reductions are -0.52 and -0.61 V vs. SHE [31] and the e^- is provided either by the electrodes in the case of electrocatalysis or by a "sacrificial donor", e.g., TEOA in the case of photocatalysis. At least for Re(I) and Ru(II) complexes, the proposed mechanism involves, in almost all cases, the formation of a coordinatively unsaturated, $17e^-$, very reactive intermediate [2]. Thus, for example, in the reduction of CO_2 using *cis*-$[Ru(bpy)_2(CO)X]^{n+}$, a mixture of $CO/HCOO^-$ is obtained [32]. Two mechanisms are proposed to operate in conjunction, having in common the very reactive, five-coordinated *cis*-$[Ru(bpy)_2(CO)]^0$ intermediate. The product selectivity depends upon the reactivity of this intermediate towards CO_2 or H^+ [2]. The so-called η^1–CO_2 *complex mechanism* operates upon CO_2 capture through the *cis*-$[Ru(bpy)_2(CO)]^0$ intermediate, forming the *cis*-$[Ru(bpy)_2(CO)(\eta^1$-$CO_2)]$ adduct, which, upon protonations, yields CO. On the other hand, in the so-called *hydride mechanism*, operating simultaneously with the η^1–CO_2 complex mechanism, the *cis*-$[Ru(bpy)_2(CO)]^0$ intermediate captures H^+, forming a hydrido intermediate, which upon reduction and CO_2 insertion into the Ru–H bond, yields $HCOO^-$. However, it should be noticed that the unsaturated five-coordinated $[Ru(bpy)_2(CO)]^0$ intermediate has not yet been detected [2]. Accordingly, there have been proposed two other mechanisms for the reduction of CO_2 [29].

Ishitani et al. [33], using various spectroscopic techniques, demonstrated the existence of the *fac*-$[Re^I(bpy)(CO)_3(OCH_2CH_2NR_2)]$ formed upon the coordination of the $TEOA^-$ anion to the metal center of the $17e^-$ five-coordinated *fac*-$[Re^I(bpy)(CO)_3]^+$ intermediate. They also demonstrated the existence of the *fac*-$[Re^I(bpy)(CO)_3(O(CO)OCH_2CH_2NR_2)]$ produced upon the insertion of CO_2 into the Re–O bond of the *fac*-$[Re^I(bpy)(CO)_3(OCH_2CH_2NR_2)]$ intermediate. A similar CO_2 insertion product has been observed also for the $[Ru(dmb)_2(CO)_2]^{2+}$ complex in DFM-TEOA solution [34]. The CO_2-into-CO reduction upon the coordination of the $TEOA^-$ anion and subsequent CO_2 insertion has also been scrutinized for Re(I) complexes with the aid of DFT calculations [35].

Finally, based upon both experimental [36,37] as well as theoretical [38] studies, there is also another proposed mechanism for CO_2 reduction using transition metal complexes, thought to operate via the dimerization of the five-coordinated, very reactive intermediate. Hence, Muckerman et al. [38], employing DFT electronic structure calculations, showed that CO_2 is inserted between two five-coordinated $[Re(dmb)(CO)_3]\cdot$ (dmb = 4,4′-dimethyl-bpy) radical intermediates, bridging their metal centers. Through a second CO_2 addition to this dimeric species, and via a transition state, CO is produced.

Although, so far, complexes of a large number of transition metals have been studied for electro/photocatalytic CO_2 reduction, Pt complexes have attracted very little attention. Ceballos et al. [39] demonstrated electrocatalytic CO_2 reduction into formate using the $[Pt(dmpe)_2](PF_6)_2$ complex with high Faradaic efficiency and low overpotential. The vast majority of studies on CO_2 reduction involving Pt metals have been devoted to heterogeneous catalysis. For example, Zhang et al. [40] dealt with the photocatalytic reduction of CO_2 into CH_4 under the influence of ultraviolet radiation, with water as solvent on a TiO_2 catalyst with Pt. Quite numerous other studies have also appeared in the literature [41–47] concerning heterogeneous CO_2 transformation. Finally, an enormous amount of work has been devoted to the ubiquitous photocatalytic water splitting for H_2 production using Pt nanoparticles [48,49].

To the best of our knowledge, neither experimental nor theoretical studies have been undertaken so far on photocatalytic CO_2-into-CO reduction employing Pt(II) square planar complexes as the catalysts. Accordingly, we instigated scrutinizing, by means of electronic structure calculations, the photocatalytic reduction of CO_2 into CO using square planar Pt(II) cyclometalated complexes bearing N^C^N-coordinating substituted dipyridylbenzene ligands of the general formula $[Pt(5$-R-$dpb)Cl]$ (dpb = 1,3-di(2-pyridyl)benzene anion, R = H, *N,N*-dimethylaniline, thiophene, bodipy). Our targets are (1) to study the photophysical properties of these complexes in order to investigate whether they could be used as both photosensitizers as well as catalysts, (2) to explore the mechanism of the

catalytic reaction and (3) to probe how the nature of the NˆCˆN-substituted bipyridyl ligand affects both the photophysical properties and mechanism of action of the Pt(II) complexes under study.

2. Results and Discussion

The molecular structure of the square planar Pt(II) complexes employed for the CO_2-into-CO photocatalytic reduction in this study is depicted in Scheme 1.
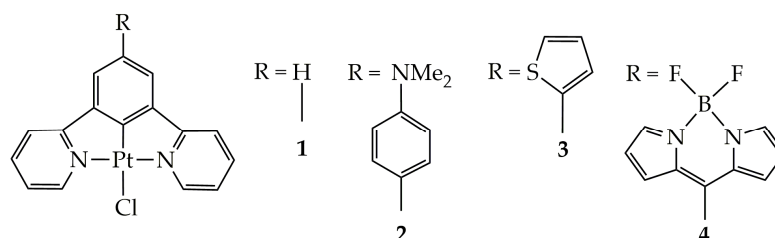
Scheme 1. The molecular structures of Pt(II) complexes under study.

The CO_2-into-CO photocatalytic reduction is thought to proceed via two steps: (1) the photoexcitation/reductive quenching step and (2) the actual catalytic cycle. The two steps are depicted in Figure 1 along with the molecular structures of all the species participating in the overall process. Let us start by examining first the initial step, which henceforth we shall call the photoexcitation/reductive quenching step, and next we will deal with the second step, which we shall call the catalytic cycle step.
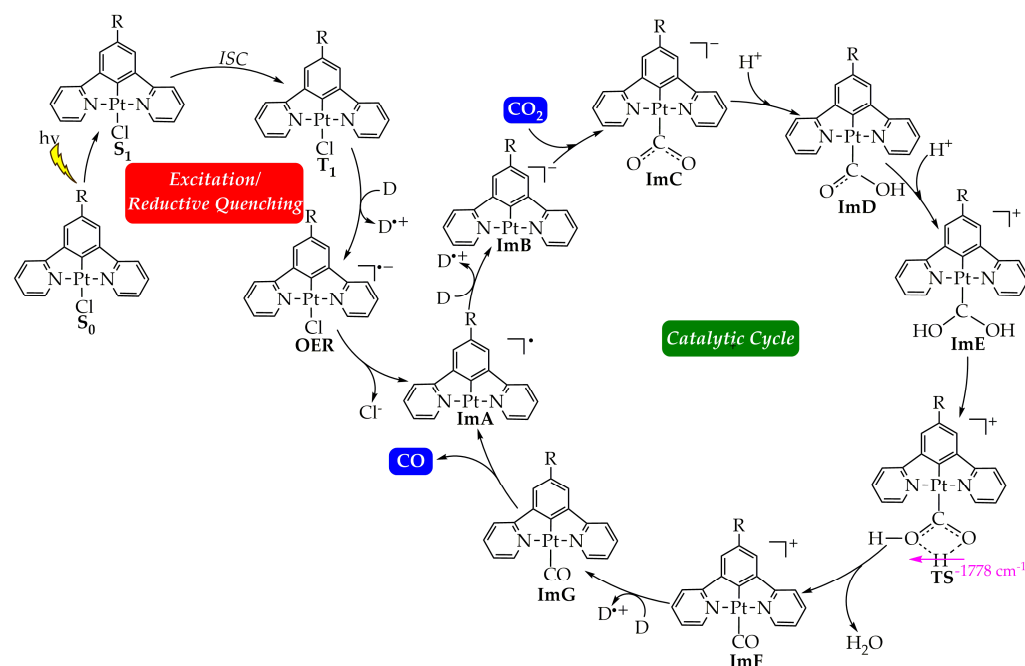

Figure 1. Proposed calculated mechanism for the CO_2-into-CO photocatalytic reduction by the [Pt(5-R-dpb)Cl], **1**–**5** Pt(II) complexes.

2.1. Photoexcitation/Reductive Quenching Step

In the first step, the Pt(II) catalyst, upon irradiation, is excited to its first singlet excited state, S_1. For a third-row transition metal complex like those under study, it is expected for the transition to occur from the S_1 state to the first triplet excited state T_1 via Intersystem Crossing (*ISC*) due to Spin–Orbit Coupling (*SOC*). Then, if the lifetime τ of the T_1 state of the complex is large enough, reductive quenching occurs, where the complex, upon accepting an e$^-$ from a donor D, e.g., TEOA or TEA, yields the One-Electron-Reduced (OER) complex

(Figure 1). Notice that the experimentally determined τ of the T_1 state of **1** has been found to be 7.2 µs in a CH_2Cl_2 solvent at 298 °C [50], which is large enough to permit reductive quenching. The optimized geometries of **1**–**4** in their S_0 and T_1 states, as well the geometries of the respective OER species, along with the selected structural parameters calculated at the PBE0-GD3BJ/Def2-TZVP level, in the DCM solvent are given in Figure 2, as well as in Figures S1–S3 of the Supplementary Materials. The calculated structural parameters of **1** in its S_0 ground state are in excellent agreement with the respective structural parameters derived from the X-ray structural analysis of this complex [51]. Thus, for example, the difference between the calculated and X-ray derived bond lengths around the coordination sphere is in the range of only 0.001–0.016 Å, while the calculated bond angles differ by only 0.3–0.5° from the respective X-ray experimental values. Upon excitation to the T_1 excited state, no significant differences in the structural parameters could be observed (Figures 2b and S1–S3). Accordingly, the changes in the Pt–Cl and Pt–C coordination bonds are in the ranges 0.03–0.001 Å and 0.009–0.019 Å, respectively, while the changes in the Pt–N coordination bond lie within the range 0.0–0.015 Å. On the other hand, the bond angles around the coordination sphere change slightly by about 1° in all cases, **1**–**4**. Finally, the same holds also for the organic framework of the N^C^N pincer ligand, where the structural changes upon $S_0 \rightarrow T_1$ excitation are negligible. Next, the one-electron reduction of the T_1 state causes more significant structural changes. Thus, there are more obvious structural differences between the optimized geometries of the T_1 state and the OER species (Figure 2c and Figures S1–S3). The most striking structural change is observed in the Pt–Cl coordination bond, which is elongated by 0.007–0.032 Å in the **OER** species as compared to the T_1 state species. The same holds also if we compare the **OER** species with the S_0 state species. Also, the Pt–C coordination bond is elongated by 0.035 Å in contrast to the two Pt–N coordination bonds, which are shortened.
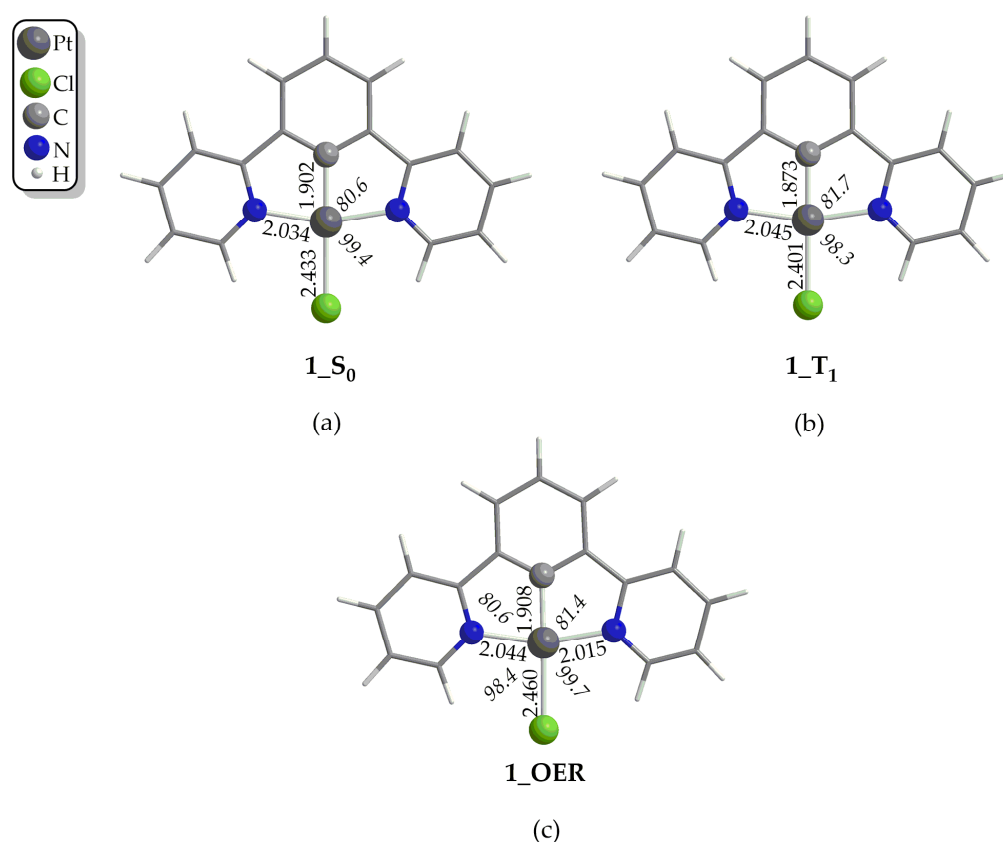

Figure 2. Optimized geometries of **1** in (**a**) S_0 ground state, (**b**) in T_1 excited state and (**c**) of One-Electron-Reduced form, **1_OER**, calculated at the PBE0-GD3BJ/Def2-TZVP level, in DCM solvent.

Finally, the bond angles around the coordination sphere do not change significantly upon one-electron reduction.

2.1.1. Absorption Spectra

Since the excitation of the precursor complexes **1–4** is a prerequisite in photocatalytic CO_2 conversion, we set out to study their absorption spectra in DCM by means of TDDFT calculations. Accordingly, we employed the two most popular functionals (vide infra), for the simulation of the absorption spectra in DCM of the complexes under study, namely PBE0 and CAM-B3LYP, using the Def2-TZVP basis set in both cases. The simulated absorption spectra of **1–4** calculated using the TDDFT/PBE0/Def2-TZVP computational protocol are depicted in Figure 3, while those obtained using the TDDFT/CAM-B3LYP/Def2-TZVP computational protocol are given in Figure S4 of the Supplementary Materials.
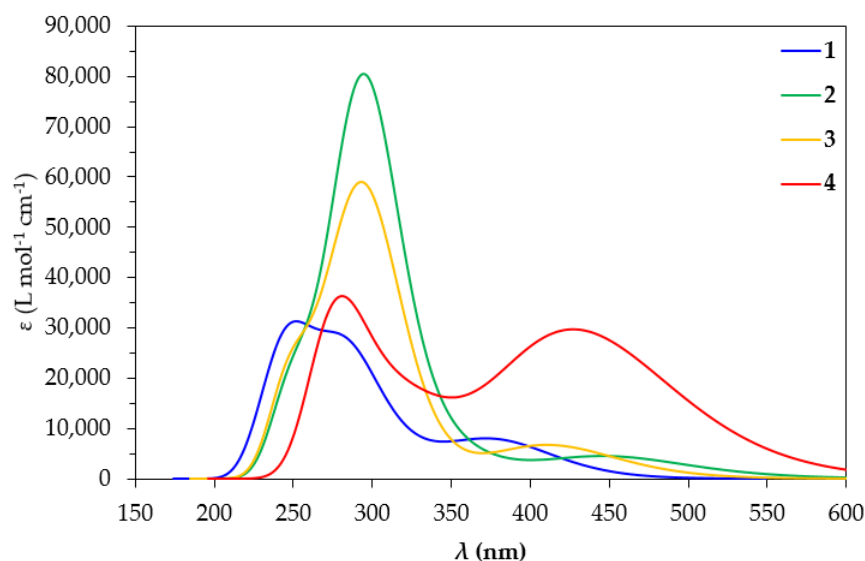

Figure 3. Simulated absorption spectra of **1–4** in DCM at the TDDFT/PBE0/Def2-TZVP level.

The simulated absorption spectrum of **1** calculated at the PBE0/Def2-TZVP level in DCM is in agreement with the experimental absorption spectrum derived by Williams et al. for **1** in DCM [50]. Thus, the simulated spectrum of **1** exhibits a band at 380 nm, reproducing excellently the experimental maximum found at 380 nm in the experimental spectrum as well. On the other hand, the simulated absorption spectrum of **1** at the CAM-B3LYP/Def2-TZVP level (Figure S4) shows a maximum at 344 nm, underestimating the experimental maximum by about 36 nm. The simulated absorption spectra using both computational protocols employed in this study exhibit also higher energy maxima below 300 nm, underestimating the respective maxima found in the experimental spectra at 330 nm and below. It should be noticed that overall, the simulated absorption spectra of **1–4** at the CAM-B3LYP/Def2-TZVP level are blue-shifted by 30–40 nm compared to those calculated at the PBE0/Def2-TZVP level in DCM. Let us further analyze the spectra calculated at the PBE0/Def2-TZVP level due to their better agreement with the experiment. Perusal of Figure 3 reveals that the simulated absorption spectra at the PBE0/Def2-TZVP level in DCM of **1**, **2**, **3** and **4** exhibit low-energy bands at 380, 460, 420 and 428 nm, respectively. In addition, the simulated absorption spectra of all complexes exhibit high-energy bands in the region of 250–300 nm.

In terms of Natural Transition Orbitals (NTOs), the band peaking at 380 nm arises mainly from an electronic transition at 381 nm, which is due to the electron excitation between the NTO pair depicted in Figure 4. Based upon the shape of these NTOs, the band shows a mixed assignment comprising of Metal-to-Ligand Charge Transfer (MLCT), Intra-Ligand (IL) and Ligand-to-Ligand Charge Transfer (LL'CT) characters (MLCT/IL/LL'CT). The same assignment holds also true for the low-energy bands in the region 420.
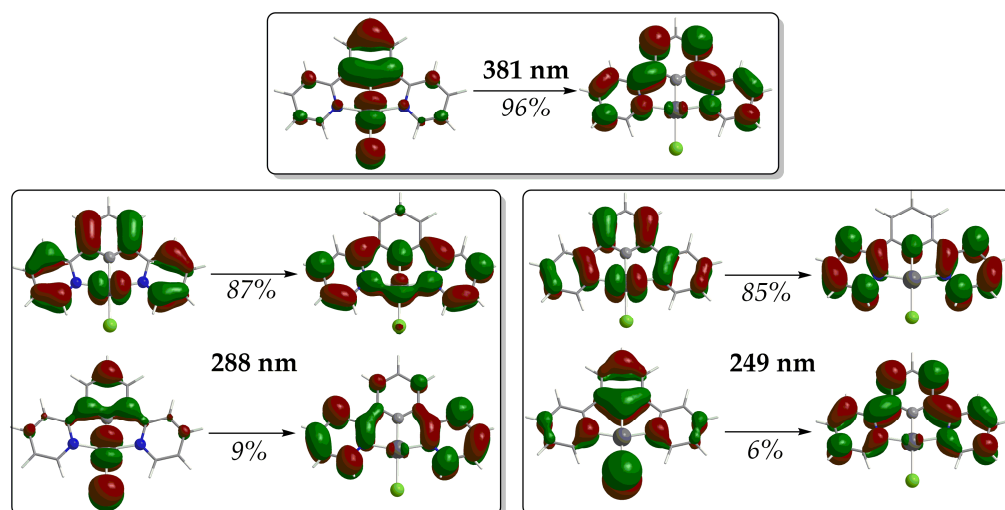
Figure 4. NTO pairs for the most significant electronic transitions of the simulated absorption spectra of **1** (hole h^+ on the left, electron e^- on the right).

The calculated absorption spectra of **2** and **3** exhibit a band around 460 nm. The former exhibits a band around 460 nm while the latter exhibits a band around 420 nm, arising from electronic transitions at 452 and 414 nm, respectively. Based upon the shapes of the NTO pairs (Figures S5 and S6 of Supplementary Materials) participating in these electronic transitions, these low-energy bands are assigned as MLCT/IL/LL'CT. The exception is complex **4**, where the band around 428 nm arises mainly from an electronic transition at 420 nm, assigned as MLCT/IL.

Next, the simulated absorption spectra exhibit high-energy bands in the UV region (Figure 3). The spectrum of complex **1** shows two such high-energy bands around 250 and 280 nm. The latter arises mainly from an electronic transition at 288 nm while the former is mainly due to an electronic transition at 249 nm. The shape of the NTOs involved in these transitions indicates that the high-energy bands in the UV are of MLCT/IL/LL'CT character. On the other hand, the absorption spectra of complexes **2–4** exhibit just one distinct high-energy band in the UV region. This high-energy band appears around 295 nm for **2** and **3** and around 284 nm for **4**. For complexes **2** and **3**, these bands are also of the highest intensity in their absorption spectra. For **2**, the most intense high-energy band arises mainly from an electronic transition at 298 nm, involving almost solely an excitation between a pair of NTOs (Figure S5). Based upon the shape of these NTOs, the band at 285 nm for **2** is assigned as MLCT/IL. Conversely, for **3**, the high-energy band arises mainly from an electronic transition at 279 nm, which is, however, due to excitations involving two NTO pairs (Figure S6). The band around 295 nm for **3** is assigned as MLCT/IL/LL'CT in accordance with the shape of the NTOs involved.

2.1.2. Excited State Electrochemistry

One of the most important steps in photocatalytic CO_2 conversion using transition metal catalysts is the reductive quenching of their T_1 state upon receiving an e from a sacrificial donor, e.g., TEOA. Therefore, we instigated studying the T_1 excited state reduction potentials using DFT calculations. The ground-state redox potentials could be calculated by employing the Born–Haber cycle [52] depicted schematically in Scheme 2.

The standard absolute ground-state reduction potential E^0_{red} is calculated using the following equation:

$$E^0_{red} = -\Delta G^\circ(\text{soln. redox})/ZF, \tag{3}$$

where F is the Faraday constant (23.061 kcal per volt gram equivalent) and Z is the unity for the one-electron redox processes. $\Delta G^\circ(\text{soln., redox})$ is obtained from the following equation:

$$\Delta G^\circ(\text{soln., redox}) = \Delta G^\circ(\text{gas, redox}) + \Delta G^\circ(\text{solv.,[Pt(5-R-dpb)Cl]}^{\bullet-}) - \Delta G^\circ(\text{solv.,[Pt(5-R-dpb)Cl], S}_0) \qquad (4)$$
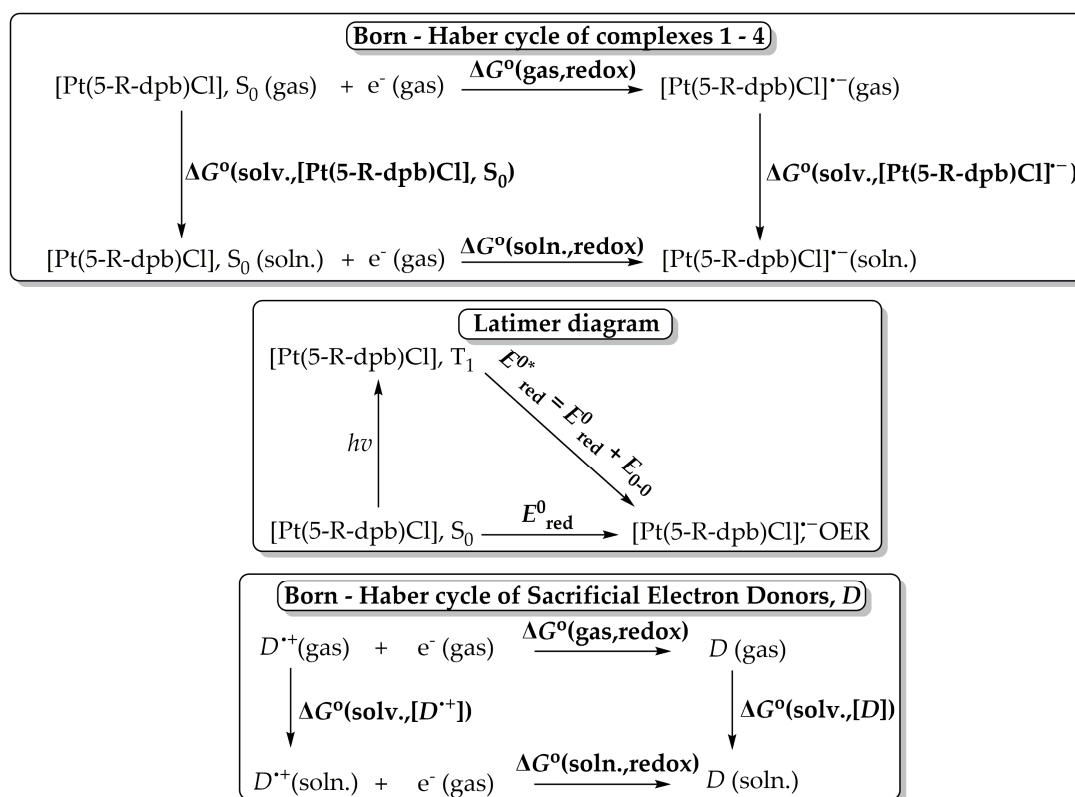
Scheme 2. Born–Haber cycle for calculation of ground-state reduction potentials E^0_{red} (**above**), Latimer diagram for the calculation of T_1 excited state reduction potentials E^{0*}_{red} (**middle**) and Born–Haber cycle for calculation of sacrificial electron donor D (=TEOA or TEA) reduction potentials (**below**).

In Table 1 are tabulated the values of the reduction potentials calculated for complexes **1–4** calculated at the PBE0/def2-TZVP level. In Table 1 are given also the reduction potentials of the sacrificial electron donors D TEOA and TEA at the same level of theory.

Table 1. Reduction potentials (in Volts) of **1–4** in S_0 state, E^0_{red}, in T_1 state, E^{0*}_{red}, along with E^0_{red} of TEOA and TEA and the respective values vs. SHE calculated at the PBE0/Def2-TZVP level.

Complex	E^0_{red}	E^{0*}_{red}	E^0_{red} vs. SHE	E^{0*}_{red} vs. SHE [1]	E^{0*}_{redox} [2]	
					vs. TEOA	vs. TEA
1	−2.48	1.80	0.32	4.60	7.43	7.19
2	−2.46	1.82	−0.36	3.92	7.45	7.21
3	−2.54	1.74	−0.34	3.94	7.37	7.13
4	−3.48	0.80	−1.88	2.40	6.43	6.19
TEOA	−5.63		−1.35			
TEA	−5.39		−1.11			

[1] SHE = Standard Hydrogen Electrode. [2] Taken as $E^0_{red}(\text{complex}) + E^0_{ox}(D)$ where $E^0_{ox}(D) = -E^0_{red}(D)$.

Inspection of Table 1 reveals that the oxidizing ability of the Pt(II) complexes in their T_1 state follows the series **2 > 1 > 3 > 4**, i.e., **2** is anticipated to accept an e⁻ in the T_1 state and be the most easily reduced amongst all the complexes under study. In contrast, the oxidizing ability of the Pt(II) complexes in their S_0 ground state follows exactly the same order as that observed for the T_1 state, following the order **2 > 1 > 3 > 4**. We could draw the

same conclusion based also upon the values of the overall redox potential E^0 calculated for the redox reaction of **1–4** in the T_1 state with TEOA or TEA, which is favorable since it is positive in all cases. The most favorable redox reaction will be with **2**, followed by **1**, **3** and **4**.

2.2. Catalytic Cycle Step

The initial photoexcitation/reductive quenching step ends with the formation of the **OER** species. The latter, upon losing a chloride ligand, yields a three-coordinated intermediate **ImA**, which starts the actual catalytic cycle (Figure 1). **ImA** could be considered the "true" catalyst while the initial Pt(II) complex could be considered a "precatalyst". Based upon earlier studies [2], the catalytic cycle step could proceed upon the one-electron reduction of **ImA** with the aid of an electron donor D like, for example, TEOA, yielding **ImB**. Next, there is one of the most important steps, i.e., the CO_2 addition to the metal center of **ImB**. After two subsequent protonations (e.g., with TEOA, which can act as proton source as well [2]), we arrive, through the transition state **TS**, to the carbonyl intermediate **ImF**. A second electron reduction of the latter yields **ImG**, from which we obtain CO and the initial "true" catalyst **ImA**.

2.2.1. The η^1–CO_2 Complex

Since the CO_2 capture/activation step, upon coordination to the metal center of the catalyst, is considered to be of paramount importance in electro/photocatalytic CO_2 conversion [53,54], we set out to study in depth the structural, bonding and electronic properties of **ImC**.

Structural Properties

The optimized geometry of **1_ImC** calculated at the PBE0-D3/Def2-TZVP level, in DCM solvent, is depicted in Figure 5a, while those of **2_ImC**, **3_ImC** and **4_ImC** are given in Figures S5–S7 of the Supplementary Material.
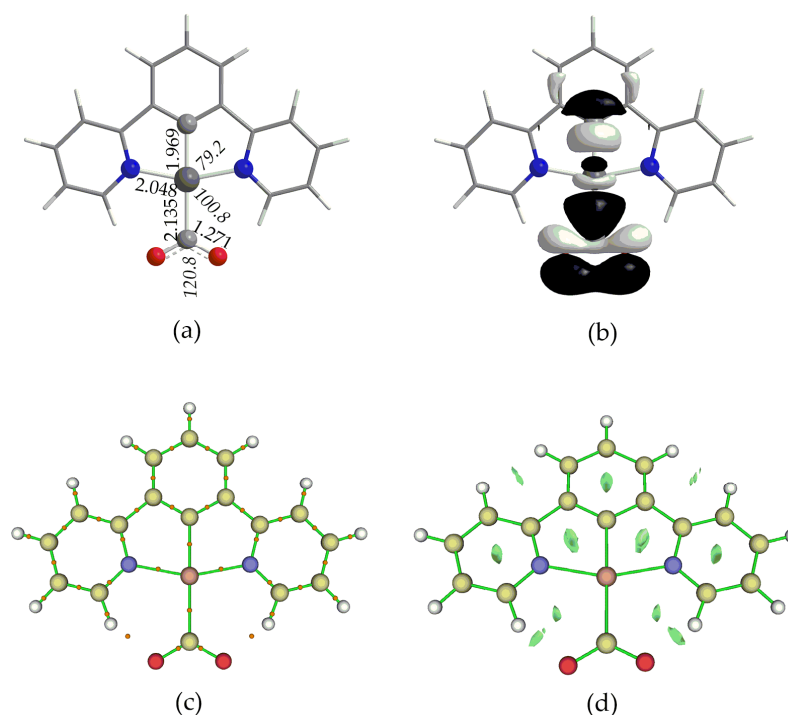

(a)

(b)

(c)

(d)

Figure 5. (**a**) Optimized geometry of **1_ImC**, (**b**) 3D surface plot of HOMO, (**c**) BCPs (orange spheres) and (**d**) 3D surface of RDG function.

Perusal of Figure 5a and Figures S5–S7 reveals that, in all complexes, CO_2 is coordinated to the Pt metal center via the C atom in an η^1-bonding mode. The complex formed via the η^1–CO_2 bonding mode is considered to be of pivotal importance to the majority of the electron transfer reactions for photo/electrocatalytic CO_2 conversion [2,53]. The Pt–CO_2 bond length is estimated to be 2.132–2.135 Å, indicative of a bonding interaction. Upon coordination to the Pt metal center, the CO_2 molecule is activated and changes from linear to bended, with a <O–C–O bond angle equal to 120.8°, while the C–O bonds are equal to 1.270 Å, elongated by about 0.110 Å as compared to the "free" CO_2 molecule (1.160 Å).

Bonding and Electronic Properties

The covalent nature of the Pt–CO_2 bond is reflected in the shape of HOMO calculated for **1_ImC** and depicted schematically in Figure 5b (the HOMOs of **2_ImC**, **3_ImC** and **4_ImC**). The HOMO is a bonding MO mainly constructed by the in-phase combination of the Pt d_{z2} AO with the π^* MO of CO_2, in line with previous studies [51]. The bond dissociation energy D_0 of the Pt–CO_2 bond was found to be −36.8, −36.9, −35.1 and −10.3 kcal/mol for **1_ImC**, **2_ImC**, **3_ImC** and **4_ImC**, respectively. Obviously, substitution into position 5 of the N^C^N pincer ligand has no significant impact on D_0(Pt–CO_2). The exception is complex **4**, where the introduction of the diazaborinine group reduces D_0(Pt–CO_2) by a third as compared to the rest of the complexes. Nevertheless, based upon the magnitude of D_0(Pt-CO_2), the interaction between **ImB** and CO_2 is expected to be a relatively favorable interaction.

To further analyze the Pt–CO_2 bond in **ImC**, we employed the atoms in molecules (AIM) method. In Figure 5c are depicted the bond-critical points (BCPs) found using the AIM method for **1_ImC** (similar BCPs are detected also for the intermediate **ImC** formed by complexes **2–4**). According to Bader's [55,56] theory, the presence of a BCP between two atoms indicates bond formation. Inspection of Figure 5c reveals the existence of a BCP between the Pt metal center and C atom of the CO_2 ligand, indicating a Pt–CO_2 bonding interaction. It has been proposed [57,58], based upon the values of certain properties of BCPs, that the bonding interactions could be classified into three categories: (a) pure closed-shell interactions (e.g., ionic bonds, hydrogen bonds and van der Waals interactions) characterized by $|V_{BCP}|/G_{BCP} < 1$ ($\nabla^2\rho_{BCP} > 0$ and $H_{BCP} > 0$); (b) pure open-shell (covalent) interactions characterized by $|V_{BCP}|/G_{BCP} > 2$ ($\nabla^2\rho_{BCP} < 0$ and $H_{BCP} < 0$) and (c) intermediate bonds with $1 < |V_{BCP}|/G_{BCP} < 2$ (i.e., $\nabla^2\rho_{BCP} > 0$ and $H_{BCP} < 0$) where V_{BCP} is the potential energy density at the BCP, G_{BCP} is the kinetic energy density at the BCP, $\nabla^2\rho_{BCP}$ is the Laplacian of electron density ρ at the BCP and finally H_{BCP} is the energy density at the BCP. Accordingly, the calculated values of these properties for the BCP found between Pt and CO_2 in intermediates **1_ImC–4_ImC** are given in Table 2.

Table 2. Topological and energetic properties of ρ(r) calculated at the (3, −1) bond-critical point (BCP) located at the Pt-CO_2 bond of intermediates **1_ImC–4_ImC**.

Species	ρ_{BCP} [1]	$\nabla\rho_{BCP}$ [2]	G_{BCP} [3]	V_{BCP} [3]	$\|V_{BCP}\|/G_{BCP}$	H_{BCP} [3]	G_{BCP}/ρ_{BCP} [4]
1_ImC	0.124	0.137	0.089	−0.145	1.629	−0.056	0.718
2_ImC	0.125	0.138	0.090	−0.147	1.633	−0.057	0.720
3_ImC	0.125	0.135	0.090	−0.147	1.633	−0.057	0.720
4_ImC	0.125	0.130	0.088	−0.145	1.648	−0.057	0.704

[1] in $e\text{Å}^{-3}$. [2] in $e\text{Å}^{-5}$. [3] in kJ mol^{-1} (atomic unit volume)$^{-1}$. [4] in kJ mol^{-1} electron^{-1}. The bond degree parameter H_{BCP}/ρ_{BCP} represents either the covalence ($H_{BCP} < 0$) or the softening ($H_{BCP} > 0$) degree of the interaction.

Inspection of Table 1 reveals that the AIM parameters calculated for the Pt–CO_2 BCP do not vary significantly between the **ImC** intermediates of **1–4**. Based upon the values of AIM parameters given in Table 1, we can assume that Pt–CO_2 interaction falls into the third category, i.e., intermediate nature arising from an interplay of covalent, electrostatic, charge transfer and probably weak dispersion force components. However, the latter should be

excluded for the Pt–CO_2 bond, in terms of the Reduced Density Gradient (RDG) defined using the following equation [59]:

$$RDG(r) = |\nabla\rho(r)| / 2(3\pi^2)^{1/3}\rho(r)^{4/3} \tag{5}$$

where $\rho(r)$ is the electron density ρ at point r. The 3D isosurface map of the RDG, depicted in Figure 5d, reveals the absence of any weak interactions between the Pt metal center and CO_2 (notice that the green isosurface represents weak interactions regions). Similar RDG maps are observed for complexes **2–4** as well. In addition, inspection of Figure 5c reveals the existence of two BCPs located between the O atoms of CO_2 and the H atoms of the NˆCˆN pincer ligand. Also, the RDG function (Figure 5d) reveals non-covalent interactions between those atoms. Therefore, these H bond interactions further contribute to the overall interaction of CO_2 with the **Im_B** intermediate.

Another useful method for analyzing the chemical bond is the NBO method, which is a partitioning scheme for the electronic charge distribution in a molecule. Thus, we employed NBO calculations to analyze the Pt–CO_2 bond from this point of view. The results of the NBO analysis are given in Table 3.

Table 3. Natural charges Q, bonding NBOs BD and hyperconjugative interaction stabilization energy $\Delta E(2)$ relevant to the Pt–CO_2 in **1_ImC–4_ImC**.

Species	Q_{Pt}	Q_C [1]	BD[σ(Pt-CO_2)]	$\Delta E(2)$	
				σ(Pt-C$_{NˆCˆN}$) → σ*(Pt-CO_2)	σ(Pt-CO_2) → σ*(Pt-C$_{NˆCˆN}$)
1_ImC	0.235	0.495	$0.558h_{Pt} + 0.830h_C$	58.3	27.8
2_ImC	0.237	0.494	$0.540h_{Pt} + 0.842h_C$	58.1	26.4
3_ImC	0.244	0.495	$0.538h_{Pt} + 0.843h_C$	58.3	27.2
4_ImC	0.260	0.497	$0.535h_{Pt} + 0.845h_C$	56.9	23.6

[1] Referring to the CO_2 carbon atom.

The natural charges obtained using NBO analysis are found to be 0.235–0.260 for Pt and 0.494–0.497 for the C atom of the CO_2 ligand. This results in a repulsive electrostatic interaction between the Pt and CO_2 in line with previous findings [53,60]. The NBO analysis reveals also the existence of a bonding BD σ NBO, which is depicted in Figure 6a for **1_ImC** (similar BD NBOs are observed also for the rest of the respective intermediates).

The linear combinations of the BD[σ(Pt–CO_2)] NBOs found for **1_ImC–4_ImC** are given in Table 2. Thus, for example, the σ(Pt–C) bonding NBO of **1_ImC** has an occupation number equal to 1.857 |e|, arising from the interaction of the sp$^{2.23}$d$^{1.08}$ hybrid orbital of Pt (23.15% s, 51.66% p and 25.03% d character) with the sp$^{1.88}$ hybrid orbital of the C donor atom of CO_2 (34.72% s and 65.25% p character), and is described as σ(Pt–C) = $0.558h_{Pt} + 0.830h_C$. In Figure 6b are also depicted the shapes of the NBOs participating in the donor– acceptor hyperconjugative interactions related to the Pt–CO_2 bond in **1_ImC**. According to NBO analysis [61], there is a stabilization of a system due to the charge transfer interactions between specific donor-acceptor NBOs. The stabilization energy, $\Delta E(2)$, arising from these hyperconjugative (stereoelectronic) interactions is given using the following equation:

$$\Delta E(2) = q_i F_{ij} / (\varepsilon_i - \varepsilon_j) \tag{6}$$

where q_i is the occupancy of the donor NBO, F_{ij} is the off-diagonal Fock matrix elements and ε_i and ε_j are the energy of the donor and acceptor NBOs, respectively. The two hyperconjugative interactions related to the Pt–CO_2 bond given in Figure 6b involve σ(Pt–C) and σ*(Pt–C) NBOs and stabilize the system overall by 86.1 kcal/mol. The overall stabilization due to hyperconjugative interactions for **2_ImC**, **3_ImC** and **4_ImC** is 84.5, 85.5 and 80.5 kcal/mol, respectively.
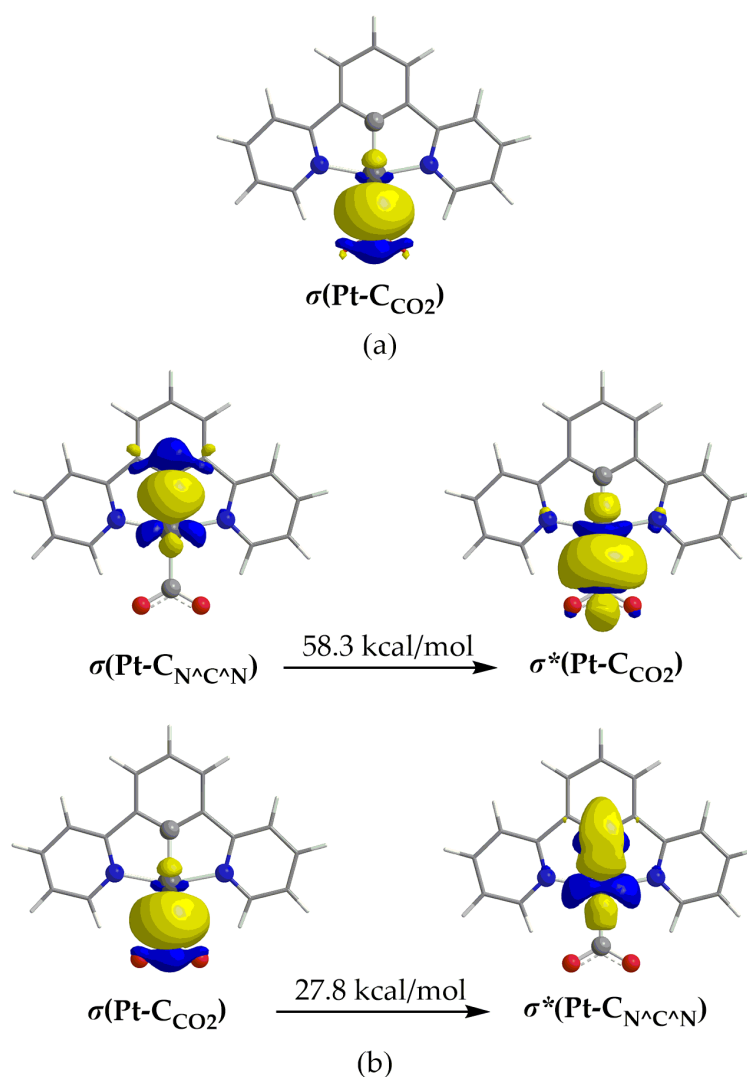
Figure 6. 3D isosurface plots of (**a**) σ(Pt–C) BD NBO and (**b**) of donor and acceptor NBOs participating in the Pt–C hyperconjugative interactions.

Another method for analyzing a chemical bond is Charge Decomposition Analysis (CDA) [62]. We employed the latter to study the Pt–CO_2 interaction for **1_ImC** as a representative case. In contrast to the Co–CO_2 interaction in Co complexes, where charge transfer has been proposed [63,64], the net charge transfer from the Pt fragment to the CO_2 is calculated to be marginal, amounting to only 0.048 |e| (the donation d and backdonation b terms were found to be -0.023 and -0.071 |e|, respectively, and are somewhat balanced). Finally, the charge polarization term r has a negative value equal to -0.350, indicating electronic charge removal from the overlapping into the non-overlapping regions upon the formation of **1_ImC**. An orbital interaction diagram for the formation of **1_ImC** from the fragments [Pt(dpb)]$^-$ (Fragm. 1) and CO_2 (Fragm. 2) is depicted in Scheme 3.

Perusal of Scheme 3 reveals that the bonding HOMO of the complex **1_ImC**, reflecting the covalent Pt-CO_2 interaction, is composed of 34% of LUFO+1 of Fragm. 1 and 55% of LUFO of Fragm. 2. In other words, the HOMO of **1_ImC** is constructed by the in-phase interaction of the, mainly of the Pt d_{z2} character, LUFO+1 of the [Pt(dpb)]$^-$ fragment, with a π^* MO of the CO_2 fragment.
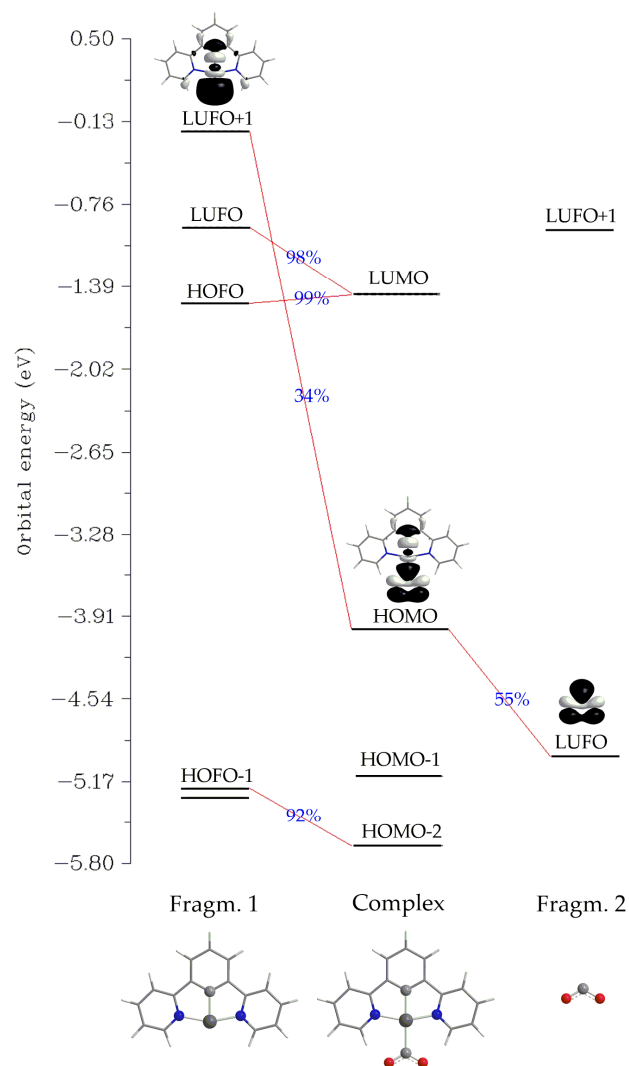
Scheme 3. Orbital interaction diagram for the formation of **1_ImC** (Complex) from fragments [Pt(dpb)]$^-$ (Fragm. 1) and CO_2 (Fragm. 2).

2.2.2. Energetic Reaction Profiles

The free energy reaction profiles calculated for **1–4**, corresponding to the respective catalytic cycle step (Figure 1), are given in Figure 7. The catalytic cycle starts with **ImA**, which is obtained from **OER** upon the loss of the chloride ligand (vide supra). Experimental studies have already proposed the loss of the halide ligand from the Re and Ru complexes used in catalytic CO_2 conversion [2]. Our study indicates that this should also hold for the Pt complexes under investigation. Therefore, the latter, upon reduction in their T_1 excited state, accept an electron in the SOMO$^\beta$ depicted in Scheme 4. Putting an electron in this antibonding MO would weaken the Pt–Cl bond, thus facilitating its dissociation. This is further corroborated by the fact that the single electron in the OER species resides on the antibonding SOMO (Scheme 4), destabilizing the Pt–Cl bond and favoring its dissociation.

Next, inspection of the energetic profiles reveals that the CO_2-into-CO conversion by the catalytically active species **ImA** is a strongly exergonic reaction. Upon reduction, **ImA** yields the reactive intermediate **ImB**, which subsequently captures a CO_2 molecule to yield the η^1–CO_2 complex **ImC**. Successive protonation of the latter results in the formation of the immensely stabilized intermediate **ImE**. Next, **ImE** is converted into the carbonyl intermediate **ImF** through a concerted mechanism and via a transition state, **TS**, surmounting an activation barrier of around 38 kcal/mol. Finally, upon a second electron reduction, we obtain CO while regenerating the catalytically active species **ImA**.
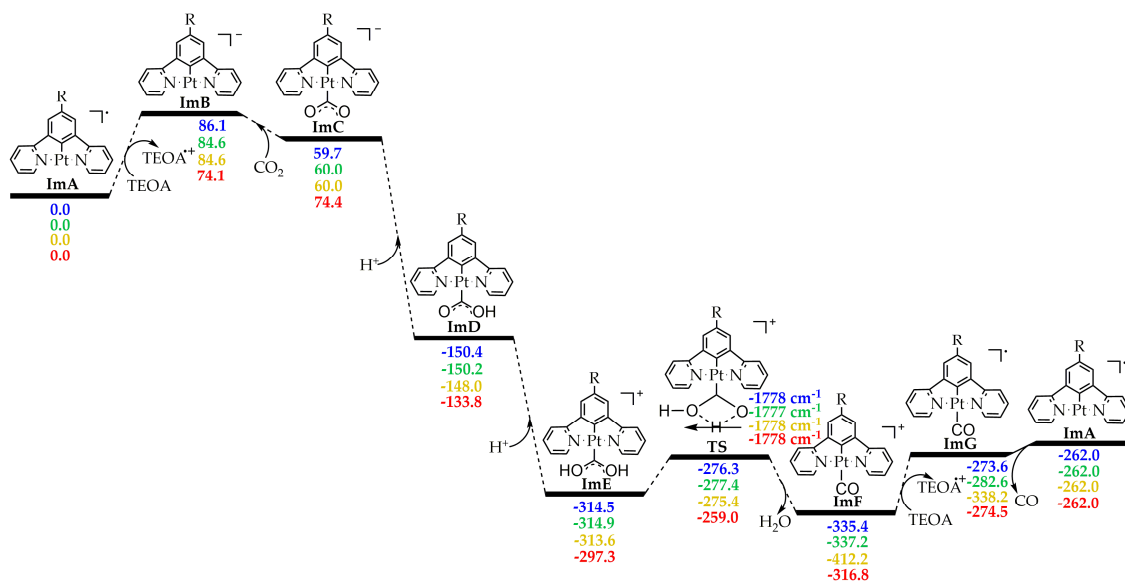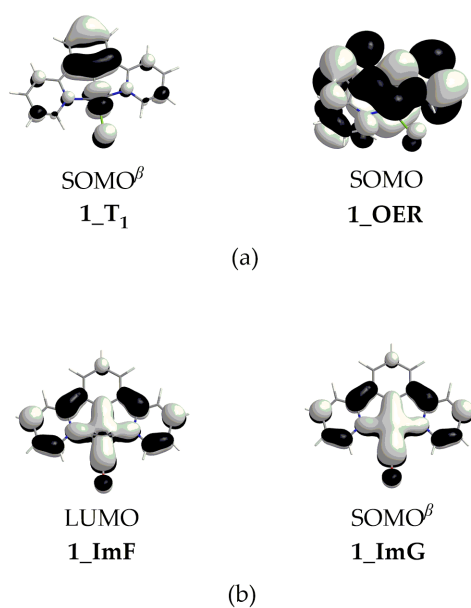
Figure 7. Free energy, ΔG (in kcal/mol), reaction profiles of **1–4** in DCM solvent calculated at the PBE0-GD3BJ/Def2-TZVP level (numbers in blue for **1**, in green for **2**, in orange for **3** and in red for **4**).

(a)

(b)

Scheme 4. (**a**) SOMO$^\beta$ of **1_T$_1$** species (**left**) and SOMO of **1_OER** (**right**) and (**b**) LUMO of **1_ImF** (**left**) and SOMO$^\beta$ of **1_G** (**right**).

It should be noticed that the dissociation of the Pt–CO upon the reduction of the **ImF** intermediate should be favorable since it accepts an electron in its antibonding LUMO (Scheme 4). Also, the single electron in the **ImG** intermediate resides on the antibonding SOMO$^\beta$ (Scheme 4), destabilizing the Pt–CO bond. These findings are in line with experimental studies proposing CO dissociation upon the reduction of various complexes acting as CO_2 reduction catalysts [2].

The optimized geometries, along with selected structural parameters, of all the intermediates and TSs involved in the catalytic cycle are given in Figures S7–S10. Perusal of the latter reveals that the substitution of one H atom of **1** by an R substituent (Scheme 1) has no significant impact on the structural parameters of the [Pt(5-R-dpb)Cl] complexes.

3. Computational Methods

Full geometry optimization has been performed for all the species under study, without symmetry constraints, using the 1997 hybrid functional of Perdew, Burke and Ernzerhof [65–70], as implemented in the program Gaussian16W [71]. This functional uses 25% exchange and 75% weighting correlation and is denoted as PBE0. Dispersion interactions were accounted for by using the D3 version of Grimme dispersion with Becke−Johnson damping [72]. The Def2-TZVP basis set for all atoms was used for the geometry optimizations. The computational protocol will be hereafter denoted as PBE0-GD3BJ/Def2-TZVP. All stationary points have been identified as minima (number of imaginary frequencies, NImag = 0). Natural bond orbital (NBO) population analysis was carried out, employing the methodology by Weinhold [63] as implemented in the G16W software, version C.01. The atoms in molecules (AIM) method of Bader [57], the reduced gradient density (RDG) method [73] and the CDA method [62] were used as implemented in the Multiwfn software, version 3.8 [74]. The Gibbs free energy was calculated to be 298.15 K and 1 atm pressure. Solvent effects were calculated using the Polarizable Continuum Model (PCM) using the integral equation formalism variant (IEF-PCM), which is the default method of G16W (self-consistent reaction field (SCRF)) [75], while Dichloromethane (DCM) was used as the solvent. Time-dependent density functional theory (TD-DFT) calculations [76–78] were performed on the ground-state S_0 equilibrium geometries in the DCM solvent employing two computational protocols, namely PBE0/Def2-TZVP and CAM-B3LYP/Def2-TZVP, taking into account the first 30 excited states. Both PBE0 and CAM-B3LYP are among the most popular functionals for the calculation of absorption spectra [79]. Also, the def2-TZVP basis set has been successfully employed for the calculation of the absorption spectra of the Pt(II) square planar complexes [80]. Finally, Natural Transition Orbitals were used, offering a greatly simplified description of the electronic transitions. [81].

4. Conclusions

The photocatalytic reduction of CO_2 into CO by [Pt(5-R-dpb)Cl] (dpb = 1,3-di(2-pyridyl)benzene anion, R = H, *N,N*-dimethylaniline, thiophene, bodipy) Pt(II) square planar complexes has been studied using DFT electronic structure calculations. The overall process is thought to proceed via two main steps: (i) photoexcitation/reduction of the initial complexes and (ii) the main catalytic cycle, producing CO. The TDDFT-simulated absorption spectra showed that these complexes exhibit strong absorptions in the range of 280–380 of the UV region, as well as weak absorptions in the range of 410–460 nm. The exception is complex **4**, with a diazaborinine-substituted NˆCˆN pincer ligand, where this phenomenon is reversed, with the strongest absorption appearing around 420 nm and the weakest around 280 nm. Thus, it is anticipated that changing the pincer ligand could provide complexes that absorb in the visible region, making them ideal for use as photocatalysts for CO_2-into-CO conversion. Next, the excited state reduction potentials, E^{0*}_{red}, dictating the reductive quenching of the Pt(II) complexes in their T_1 state have been calculated using DFT. Based upon the E^{0*}_{red} values, we conclude that the oxidizing ability of the Pt(II) complexes in their T_1 state follows the series **2 > 1 > 3 > 4**, meaning that **2** is expected to be more easily reduced amongst all the complexes under study. In general, based upon the calculated redox potentials E^{0*}_{redox} in the range of 6–8 V, all the complexes are expected to be easily reduced with a sacrificial electron donor such as TEOA or TEA. During reduction, the complexes **1**–**4** in the T_1 state accept an e$^-$ in their SOMO, being antibonding in the region of the Pt–Cl bond. In the **OER** product species, resulting from the reduction of the T_1 state complexes, the single e$^-$ resides also in an antibonding SOMO, destabilizing and facilitating the Pt–Cl bond dissociation process.

The second step of photocatalytic CO_2-into-CO conversion, namely the catalytic cycle, starts with a three-coordinated Pt(II) **ImA** intermediate, obtained from **OER** upon Pt–Cl dissociation. Upon one-e$^-$ reduction, ImA captures CO_2, and after successive protonations and reductions, yields CO. The latter is obtained from **ImF**, which accepts an e$^-$ in its LUMO, being antibonding in the region of the Pt–CO bond, while this e$^-$ resides in a

similar antibonding SOMO of the reduced **ImG** intermediate. Consequently, the Pt–CO bond is expected to be broken in the final stage of the catalytic cycle.

The Pt–CO_2 bond of the **ImC** intermediate, crucial to the overall process, has been scrutinized. It is revealed that this bond is relatively strong with D_0 in the range of −36.9−−10.3 kcal/mol, exhibiting a complex nature comprising mainly covalent and hyperconjugative interactions, which compensate for the repulsive electrostatic interactions. The Pt–CO_2 bond involves also H bonding with the NˆCˆN pincer ligand. Overall, the catalytic cycle is estimated to be a strongly exergonic process. Taking into account that **1** exhibits a very high T_1 excited state lifetime τ, a whole new series of Pt(II) complexes could be synthesized bearing suitable pincer ligands in order to absorb in the visible range, making them ideal for CO_2-into-CO conversion using sunlight.

Supplementary Materials: The following supporting information can be downloaded at: https://www.mdpi.com/article/10.3390/molecules29020403/s1, Figure S1: Optimized geometries of **2** in S_0 ground state **2_S_0**, in T_1 excited state **2_T_1** and of One-Electron-Reduced form **2_OER**, calculated at the PBE0-GD3BJ/Def2-TZVP levels in DCM solvent. Figure S2: Optimized geometries of **3** in S_0 ground state **3_S_0**, in T_1 excited state **3_T_1** and of One-Electron-Reduced form **3_OER**, calculated at the PBE0-GD3BJ/Def2-TZVP levels in DCM solvent. Figure S3: Optimized geometries of **4** in S_0 ground state **4_S_0**, in T_1 excited state **4_T_1** and of One-Electron-Reduced form **4_OER**, calculated at the PBE0-GD3BJ/Def2-TZVP levels in DCM solvent. Figure S4: Simulated absorption spectra of **1**–**4** in DCM at the TDDFT/CAM-B3LYP/Def2-TZVP levels. Figure S5: NTO pairs for the most significant electronic transitions of the simulated absorption spectra of **2** calculated at TDDFT/PBE0/Def2-TZVP levels (hole h^+ on the left, electron e^- on the right). Figure S6: NTO pairs for the most significant electronic transitions of the simulated absorption spectra of **3** calculated at TDDFT/PBE0/Def2-TZVP levels (hole h^+ on the left, electron e^- on the right). Figure S7: NTO pairs for the most significant electronic transitions of the simulated absorption spectra of **4** calculated at TDDFT/PBE0/Def2-TZVP levels (hole h^+ on the left, electron e^- on the right). Figure S8: Optimized geometries of all species involved in the catalytic cycle of CO_2-into-CO conversion by **1** calculated at the PBE0-GD3BJ/Def2-TZVP levels in DCM solvent. Figure S9: Optimized geometries of all species involved in the catalytic cycle of CO_2-into-CO conversion by **2** calculated at the PBE0-GD3BJ/Def2-TZVP levels in DCM solvent. Figure S10: Optimized geometries of all species involved in the catalytic cycle of CO_2-into-CO conversion by **3** calculated at the PBE0-GD3BJ/Def2-TZVP levels in DCM solvent. Figure S11: Optimized geometries of all species involved in the catalytic cycle of CO_2-into-CO conversion by **4** calculated at the PBE0-GD3BJ/Def2-TZVP levels in DCM solvent. Table S1: Cartesian coordinates and energetic data of the optimized geometries of all species calculated at the PBE0-GD3BJ/Def2-TZVP levels in DCM solvent.

Author Contributions: Conceptualization, A.T.; validation, A.T.; formal analysis, A.T. and A.S.; investigation, A.T. and A.S.; data curation, A.T. and A.S.; writing—original draft preparation, A.T. and A.S.; writing—review and editing, A.T.; visualization, A.T. and A.S.; supervision, A.T.; project administration, A.T. All authors have read and agreed to the published version of the manuscript.

Data Availability Statement: The data presented in this study are available in article and Supplementary Materials.

Conflicts of Interest: The authors declare no conflicts of interest.

References

1. Lahijani, P.; Zainal, Z.A.; Mohammadi, M.; Mohamed, A.R. Conversion of the greenhouse gas CO_2 to the fuel gas CO via the Boudouard reaction: A review. *Renew. Sustain. Energy Rev.* **2015**, *41*, 615–632. [CrossRef]
2. Kuramochi, Y.; Ishitani, O.; Ishida, H. Reaction mechanisms of catalytic photochemical CO_2 reduction using Re(I) and Ru(II) complexes. *Coord. Chem. Rev.* **2018**, *373*, 333–356. [CrossRef]
3. Cokoja, M.; Bruckmeier, C.; Rieger, B.; Herrmann, W.A.; Kühn, F.E. Transformation of carbon dioxide with homogeneous transition-metal catalysts: A molecular solution to a global challenge? *Angew. Chemie Int. Ed.* **2011**, *50*, 8510–8537. [CrossRef] [PubMed]

4. Monticelli, S.; Talbot, A.; Gotico, P.; Caillé, F.; Loreau, O.; Del Vecchio, A.; Malandain, A.; Sallustrau, A.; Leibl, W.; Aukauloo, A.; et al. Unlocking full and fast conversion in photocatalytic carbon dioxide reduction for applications in radio-carbonylation. *Nat. Comm.* **2023**, *14*, 4451–4461. [CrossRef] [PubMed]

5. Morris, A.J.; Meyer, G.J.; Fujita, E. Molecular approaches to the photocatalytic reduction of carbon dioxide for solar fuels. *Acc. Chem. Res.* **2009**, *42*, 1983–1994. [CrossRef] [PubMed]

6. Benson, E.E.; Kubiak, C.P.; Sathrum, A.J.; Smieja, J.M. Electrocatalytic and homogeneous approaches to conversion of CO_2 to liquid fuels. *Chem. Soc. Rev.* **2009**, *38*, 89–99. [CrossRef] [PubMed]

7. Takeda, H.; Koike, K.; Morimoto, T.; Inumaru, H.; Ishitani, O. Photochemistry and photocatalysis of rhenium(I) diimine complexes. *Adv. Inorg. Chem.* **2011**, *63*, 137–186.

8. Costentin, C.; Robert, M.; Savéant, J.M. Catalysis of the electrochemical reduction of carbon dioxide. *Chem. Soc. Rev.* **2013**, *42*, 2423–2436. [CrossRef]

9. Das, S.; Wan Daud, W.M.A. Photocatalytic CO_2 transformation into fuel: A review on advances in photocatalyst and photoreactor. *Renew. Sustain. Energy Rev.* **2014**, *39*, 765–805. [CrossRef]

10. Vandezande, J.E.; Schaefer, H.F. CO_2 Reduction Pathways on $MnBr(N-C)(CO)_3$ Electrocatalysts. *Organometallics* **2018**, *37*, 337–342. [CrossRef]

11. Paquin, F.; Rivnay, J.; Salleo, A.; Stingelin, N.; Silva, C. Multi-phase semicrystalline microstructures drive exciton dissociation in neat plastic semiconductors. *J. Mater. Chem. C* **2015**, *3*, 10715–10722. [CrossRef]

12. Yang, C.; Wang, Y.; Qian, L.; Al-Enizi, A.M.; Zhang, L.; Zheng, G. Heterogeneous Electrocatalysts for CO_2 Reduction. *Appl. Energy Mater.* **2021**, *4*, 1034–1044. [CrossRef]

13. Li, K.; Peng, B.; Peng, T. Recent Advances in Heterogeneous Photocatalytic CO_2 Conversion to Solar Fuels. *ACS Catal.* **2016**, *6*, 7485–7527. [CrossRef]

14. Ishida, H. Electrochemical/Photochemical CO_2 Reduction Catalyzed by Transition Metal Complexes. In *Carbon Dioxide Chemistry, Capture and Oil Recovery*; Iyad, K., Shaya, J., Srour, H., Eds.; InTechOpen Ltd.: London, UK, 2018; pp. 17–40.

15. Boutin, E.; Merakeb, L.; Ma, B.; Boudy, B.; Wang, M.; Bonin, J.; Anxolabèhère-Mallart, E.; Robert, M. Molecular catalysis of CO_2 reduction: Recent advances and perspectives in electrochemical and light-driven processes with selected Fe, Ni and Co aza macrocyclic and polypyridine complexes. *Chem. Soc. Rev.* **2020**, *49*, 5772–5809. [CrossRef] [PubMed]

16. Chapovetsky, A.; Do, T.H.; Haiges, R.; Takase, M.K.; Marinescu, S.C. Proton-Assisted Reduction of CO_2 by Cobalt Aminopyridine Macrocycles. *J. Am. Chem. Soc.* **2016**, *138*, 5765–5768. [CrossRef] [PubMed]

17. Chapovetsky, A.; Welborn, M.; Luna, J.M.; Haiges, R.; Miller, T.F.; Marinescu, S.C. Pendant Hydrogen-Bond Donors in Cobalt Catalysts Independently Enhance CO_2 Reduction. *ACS Cent. Sci.* **2018**, *4*, 397–404.

18. Costentin, C.; Robert, M.; Saveant, J.M.; Tatin, A. Efficient and selective molecular catalyst for the CO_2-to-CO electrochemical conversion in water. *Proc. Natl. Acad. Sci. USA* **2015**, *112*, 6882–6886. [CrossRef] [PubMed]

19. Furuya, N.; Matsui, K. Electroreduction of carbon dioxide on gas-diffusion electrodes modified by metal phthalocyanines. *J. Electroanal. Chem.* **1989**, *271*, 181–190. [CrossRef]

20. Fernández, S.; Franco, F.; Casadevall, C.; Martin-Diaconescu, V.; Luis, J.M.; Lloret-Fillol, J. A Unified Electro- and Photocatalytic CO_2 to CO Reduction Mechanism with Aminopyridine Cobalt Complexes. *J. Am. Chem. Soc.* **2020**, *142*, 120–133. [CrossRef]

21. Guo, Z.; Cheng, S.; Cometto, C.; Anxolabéhère-Mallart, E.; Ng, S.-M.; Ko, C.C.; Liu, G.; Chen, L.; Robert, M.; Lau, T.-C. Highly Efficient and Selective Photocatalytic CO_2 Reduction by Iron and Cobalt Quaterpyridine Complexes. *J. Am. Chem. Soc.* **2016**, *138*, 9413–9416. [CrossRef]

22. Tinnemans, A.H.A.; Koster, T.P.M.; Thewissen, D.H.M.W.; Mackor, A. Tetraaza-macrocyclic cobalt(II) and nickel(II) complexes as electron-transfer agents in the photo(electro)chemical and electrochemical reduction of carbon dioxide. *Recl. Trav. Chim. Pays-Bas* **1984**, *103*, 288–295. [CrossRef]

23. Beley, M.; Collin, J.-P.; Ruppert, R.; Sauvage, J.-P. Nickel (II)-cyclam: An extremely selective electrocatalyst for reduction of CO_2 in water. *J. Chem. Soc. Chem. Commun.* **1984**, 1315–1316. [CrossRef]

24. Beley, M.; Collin, J.-P.; Ruppert, R.; Sauvage, J.-P. Electrocatalytic reduction of carbon dioxide by nickel $cyclam^{2+}$ in water: Study of the factors affecting the efficiency and the selectivity of the process. *J. Am. Chem. Soc.* **1986**, *108*, 7461–7467. [CrossRef]

25. Collin, J.-P.; Jouaiti, A.; Sauvage, J.-P. Electrocatalytic properties of (tetraazacyclotetradecane) nickel (2+) and $Ni_2(biscyclam)^{4+}$ with respect to carbon dioxide and water reduction. *Inorg. Chem.* **1988**, *27*, 1986–1990. [CrossRef]

26. Nandal, N.; Jain, S.L. A review on progress and perspective of molecular catalysis in photoelectrochemical reduction of CO_2. *Coord. Chem. Rev.* **2022**, *451*, 214271. [CrossRef]

27. Lehn, J.-M; Ziessel, R. Photochemical generation of carbon monoxide and hydrogen by reduction of carbon dioxide and water under visible light irradiation. *Proc. Natl. Acad. Sci. USA* **1982**, *79*, 701–704. [CrossRef]

28. Hawecker, J.; Lehn, J.-M.; Ziessel, R. Efficient photochemical reduction of CO_2 to CO by visible light irradiation of systems containing $Re(bipy)(CO)_3X$ or $Ru(bipy)_3^{2+}$–Co^{2+} combinations as homogeneous catalysts. *Chem. Commun.* **1983**, 536–538. [CrossRef]

29. Hawecker, J.; Lehn, J.-M.; Ziessel, R. Photochemical and Electrochemical Reduction of Carbon Dioxide to Carbon Monoxide Mediated by (2,2′-Bipyridine)tricarbonylchlororhenium(I) and Related Complexes as Homogeneous Catalysts. *Helv. Chim. Acta* **1986**, *69*, 1990–2012. [CrossRef]

30. Elgrishi, N.; Chambers, M.B.; Wang, X.; Fontecave, M. Molecular polypyridine-based metal complexes as catalysts for the reduction of CO_2. *Chem. Soc. Rev.* **2017**, *46*, 761–796. [CrossRef]

31. Yamazaki, Y.; Takeda, H.; Ishitani, O. Photocatalytic reduction of CO_2 using metal complexes. *J. Photochem. Photobiol. C Photochem. Rev.* **2015**, *25*, 106–137. [CrossRef]

32. Voyame, P.; Toghill, K.E.; Méndez, M.A.; Girault, H.H. Photoreduction of CO_2 Using $[Ru(bpy)_2(CO)L]^{n+}$ Catalysts in Biphasic Solution/Supercritical CO_2 Systems. *Inorg. Chem.* **2013**, *52*, 10949–10957. [CrossRef]

33. Morimoto, T.; Nakajima, T.; Sawa, S.; Nakanishi, R.; Imori, D.; Ishitani, O. CO_2 Capture by a Rhenium(I) Complex with the Aid of Triethanolamine. *J. Am. Chem. Soc.* **2013**, *135*, 16825–16828. [CrossRef] [PubMed]

34. Tamaki, Y.; Morimoto, T.; Koike, K.; Ishitani, O. Photocatalytic CO_2 reduction with high turnover frequency and selectivity of formic acid formation using Ru(II) multinuclear complexes. *Proc. Natl. Acad. Sci. USA* **2012**, *109*, 15673–15678. [CrossRef] [PubMed]

35. Tsipis, A.C.; Sarantou, A.A. DFT insights into the photocatalytic reduction of CO_2 to CO by Re(I) complexes: The crucial role of the triethanolamine "magic" sacrificial electron donor. *Dalton Trans.* **2021**, *50*, 14797–14809. [CrossRef] [PubMed]

36. Hayashi, Y.; Kita, S.; Brunschwig, B.S.; Fujita, E. Involvement of a Binuclear Species with the Re-C(O)O-Re Moiety in CO_2 Reduction Catalyzed by Tricarbonyl Rhenium(I)Complexes with Diimine Ligands: Strikingly Slow Formation of the Re-Re and Re-C(O)O-Re Species from $Re(dmb)(CO)_3S$ (dmb = 4,4'-Dimethyl-2,2'-bipyridine, S = Solvent). *J. Am. Chem. Soc.* **2003**, *125*, 11976–11987. [PubMed]

37. Sullivan, B.P.; Bolinger, C.M.; Conrad, D.; Vining, W.J.; Meyer, T.J. One- and Two-electron Pathways in the Electrocatalytic Reduction of CO_2 by *fac*-$Re(bpy)(CO)_3Cl$ (bpy = 2,2'-bipyridine). *J. Chem. Soc. Chem. Commun.* **1985**, *20*, 1414–1416. [CrossRef]

38. Agarwal, J.; Fujita, E.; Schaefer, H.F., III; Muckerman, J.T. Mechanisms for CO Production from CO_2 Using Reduced Rhenium Tricarbonyl Catalysts. *J. Am. Chem. Soc.* **2012**, *134*, 5180–5186. [CrossRef]

39. Ceballos, B.M.; Yang, J.Y. Directing the reactivity of metal hydrides for selective CO_2 reduction. *Proc. Natl. Acad. Sci. USA* **2018**, *115*, 12686–12691. [CrossRef]

40. Zhang, Q.H.; Han, W.D.; Hong, Y.J.; Yu, J.G. Photocatalytic reduction of CO_2 with H_2O on Pt-loaded TiO_2 catalyst. *Catal. Today* **2009**, *148*, 335–340. [CrossRef]

41. Wang, W.; An, W.; Ramalingam, B.; Mukherjee, S.; Niedzwiedzki, D.M.; Gangopadhyay, S.; Biswas, P. Size and Structure Matter: Enhanced CO_2 Photoreduction Efficiency by Size-Resolved Ultrafine Pt Nanoparticles on TiO_2 Single Crystals. *J. Am. Chem. Soc.* **2012**, *134*, 11276–11281. [CrossRef]

42. Katsumata, K.I.; Sakai, K.; Ikeda, K.; Carja, G.; Matsushita, N.; Okada, K. Preparation and photocatalytic reduction of CO_2 on noble metal (Pt, Pd, Au) loaded Zn-Cr layered double hydroxides. *Mater. Lett.* **2013**, *107*, 138–140. [CrossRef]

43. Xie, S.; Wang, Y.; Zhang, Q.; Fan, W.; Denga, W.; Wang, Y. Photocatalytic reduction of CO_2 with H_2O: Significant enhancement of the activity of Pt–TiO_2 in CH_4 formation by addition of MgO. *Chem. Commun.* **2013**, *49*, 2451–2453. [CrossRef] [PubMed]

44. Xiong, Z.; Lei, Z.; Kuang, C.C.; Chen, X.; Gong, B.; Zhao, Y.; Zhang, J.; Zheng, C.; Wu, J.C.S. Selective photocatalytic reduction of CO_2 into CH_4 over Pt-Cu_2O TiO_2 nanocrystals: The interaction between Pt and Cu_2O cocatalysts. *Appl. Catal. B Environ.* **2017**, *202*, 695–703. [CrossRef]

45. Kočí, K.; Dang Van, H.; Edelmannová, M.; Reli, M.; Wu, J.C.S. Photocatalytic reduction of CO_2 using Pt/C_3N_4 photocatalyts. *Appl. Surf. Sci.* **2020**, *503*, 144426. [CrossRef]

46. Tasbihi, M.; Kočí, K.; Edelmannová, M.; Troppová, I.; Reli, M.; Schomäcker, R. Pt/TiO_2 photocatalysts deposited on commercial support for photocatalytic reduction of CO_2. *J. Photochem. Photobiol. A Chem.* **2018**, *366*, 72–80. [CrossRef]

47. Xu, J.; Liu, X.; Zhou, Z.; Deng, L.; Liu, L.; Xu, M. Platinum Nanoparticles with Low Content and High Dispersion over Exfoliated Layered Double Hydroxide for Photocatalytic CO_2 Reduction. *Energy Fuels* **2021**, *35*, 10820–10831. [CrossRef]

48. Li, X.; Bi, W.; Zhang, Q.; Tao, S.; Chu, W.; Zhang, Q.; Luo, Y.; Wu, C.; Xie, Y. Single-atom Pt as co-catalyst for enhanced photocatalytic H_2 evolution. *Adv. Mater.* **2016**, *28*, 2427–2431. [CrossRef]

49. Cao, Y.; Wang, D.; Lin, Y.; Liu, W.; Cao, L.; Liu, X.; Zhang, W.; Mou, X.; Fang, S.; Shen, X.; et al. Single Pt atom with highly vacant d-orbital for accelerating photocatalytic H2 evolution. *ACS Appl. Energy Mater.* **2018**, *1*, 6082–6088. [CrossRef]

50. Williams, J.A.G.; Beeby, A.; Davies, S.; Weinstein, J.A.; Wilson, C. An Alternative Route to Highly Luminescent Platinum(II) Complexes: Cyclometalation with NˆCˆN-Coordinating Dipyridylbenzene Ligands. *Inorg. Chem.* **2003**, *42*, 8609–8611. [CrossRef]

51. Cárdenas, D.J.; Echavarren, A.M.; Ramírez de Arellano, M.C. Divergent Behavior of Palladium(II) and Platinum(II) in the Metalation of 1,3-Di(2-pyridyl)benzene. *Organometallics* **1999**, *18*, 3337–3341. [CrossRef]

52. Demissie, T.B.; Ruud, K.; Hansen, J.H. DFT as a Powerful Predictive Tool in Photoredox Catalysis: Redox Potentials and Mechanical Analysis. *Organometallics* **2015**, *34*, 4218–4228. [CrossRef]

53. Grice, K.A. Carbon dioxide reduction with homogenous early transition metal complexes: Opportunities and challenges for developing CO_2 catalysis. *Coord. Chem. Rev.* **2017**, *336*, 78–95. [CrossRef]

54. Kinzel, N.W.; Werl, C.; Leitner, W. Transition Metal Complexes as Catalysts for the Electroconversion of CO_2: An Organometallic Perspective. *Angew. Chem. Int. Ed.* **2021**, *60*, 11628–11686. [CrossRef] [PubMed]

55. Bader, R.F.W. *Atoms in Molecules—A Quantum Theory*; Oxford University Press: Oxford, UK, 1990.

56. Bader, R.F.W. A Bond Path: A Universal Indicator of Bonded Interactions. *J. Phys. Chem. A* **1998**, *102*, 7314–7323. [CrossRef]

57. Macchi, P.; Sironi, A. Chemical bonding in transition metal carbonyl clusters: Complementary analysis of theoretical and experimental electron densities. *Coord. Chem. Rev.* **2003**, *383*, 238–239. [CrossRef]

58. Espinosa, E.; Alkorta, I.; Elguero, J.; Molins, E. From weak to strong interactions: A comprehensive analysis of the topological and energetic properties of the electron density distribution involving X–H···F–Y systems. *J. Chem. Phys.* **2002**, *117*, 5529–5542. [CrossRef]

59. Johnson, E.R.; Shahar Keinan, S.; Mori-Sánchez, P.; Contreras-García, J.; Cohen, A.J.; Yang, W. Revealing Noncovalent Interactions. *J. Am. Chem. Soc.* **2010**, *132*, 6498–6506. [CrossRef]

60. Yin, X.; Moss, J.R. Recent developments in the activation of carbon dioxide by metal complexes. *Coord. Chem. Rev.* **1999**, *181*, 27–59. [CrossRef]

61. Reed, A.E.; Curtiss, L.A.; Weinhold, F. Intermolecular Interactions from a Natural Bond Orbital, Donor-Acceptor Viewpoint. *Chem. Rev.* **1988**, *88*, 899–926. [CrossRef]

62. Dapprich, S.; Frenking, G. Investigation of Donor-Acceptor Interactions: A Charge Decomposition Analysis Using Fragment Molecular Orbitals. *J. Phys. Chem.* **1995**, *99*, 9352–9362. [CrossRef]

63. Sheng, H.; Frei, H. Direct Observation by Rapid-Scan FT-IR Spectroscopy of Two-Electron-Reduced Intermediate of Tetraaza Catalyst $[Co^{II}N_4H(MeCN)]^{2+}$ Converting CO_2 to CO. *J. Am. Chem. Soc.* **2016**, *138*, 9959–9967. [CrossRef] [PubMed]

64. Call, A.; Cibian, M.; Yamamoto, K.; Nakazono, T.; Yamauchi, K.; Sakai, K. Highly Efficient and Selective Photocatalytic CO_2 Reduction to CO in Water by a Cobalt Porphyrin Molecular Catalyst. *ACS Catal.* **2019**, *9*, 4867–4874. [CrossRef]

65. Vetere, V.; Adamo, C.; Maldivi, P. Performance of the 'parameter free' PBE0 functional for the modeling of molecular properties of heavy metals. *Chem. Phys. Lett.* **2000**, *325*, 99–105. [CrossRef]

66. Adamo, C.; Barone, V. Inexpensive and accurate predictions of optical excitations in transition-metal complexes: The TDDFT/PBE0 route. *Theor. Chem. Acc.* **2000**, *105*, 169–172. [CrossRef]

67. Adamo, C.; Barone, V. Toward reliable density functional methods without adjustable parameters: The PBE0 model. *J. Chem. Phys.* **1999**, *110*, 6158–6170. [CrossRef]

68. Ernzerhof, M.; Scuseria, G.E. Assessment of the Perdew–Burke–Ernzerhof exchange-correlation functional. *J. Chem. Phys.* **1999**, *110*, 5029–5036. [CrossRef]

69. Adamo, C.; Scuseria, G.E.; Barone, V. Accurate excitation energies from time-dependent density functional theory: Assessing the PBE0 model. *J. Chem. Phys.* **1999**, *111*, 2889–2899. [CrossRef]

70. Adamo, C.; Barone, V. Toward reliable adiabatic connection models free from adjustable parameters. *Chem. Phys. Lett.* **1997**, *274*, 242–250. [CrossRef]

71. Frisch, M.J.; Trucks, G.W.; Schlegel, H.B.; Scuseria, G.E.; Robb, M.A.; Cheeseman, J.R.; Scalmani, G.; Barone, V.; Petersson, G.A.; Nakatsuji, H.; et al. *Gaussian 16W*, Revision C.01; Gaussian, Inc.: Wallingford, CT, USA, 2016.

72. Grimme, S.; Ehrlich, S.; Goerigk, L. Effect of the damping function in dispersion corrected density functional theory. *J. Comput. Chem.* **2011**, *32*, 1456–1465. [CrossRef]

73. Wu, P.; Chaudret, R.; Hu, X.; Yang, W. Noncovalent Interaction Analysis in Fluctuating Environments. *J. Chem. Theory Comput.* **2013**, *9*, 2226–2234. [CrossRef]

74. Lu, T.; Chen, F. Multiwfn: A multifunctional wavefunction analyser. *J. Comput. Chem.* **2012**, *33*, 580–592. [CrossRef] [PubMed]

75. Tomasi, J.; Mennucci, B.; Cammi, R. Quantum Mechanical Continuum Solvation Models. *Chem. Rev.* **2005**, *105*, 2999–3093. [CrossRef] [PubMed]

76. Van Gisbergen, S.J.A.; Kootstra, F.; Schipper, P.R.T.; Gritsenko, O.V.; Snijders, J.G.; Baerends, E.J. Density-functional-theory response-property calculations with accurate exchange-correlation potentials. *Phys. Rev. A At. Mol. Opt. Phys.* **1998**, *57*, 2556–2571. [CrossRef]

77. Jamorski, C.; Casida, M.E.; Salahub, D.R. Dynamic polarizabilities and excitation spectra from a molecular implementation of time-dependent density-functional response theory: N_2 as a case study. *J. Chem. Phys.* **1996**, *104*, 5134–5147. [CrossRef]

78. Bauernschmitt, R.; Ahlrichs, R. Treatment of electronic excitations within the adiabatic approximation of time dependent density functional theory. *Chem. Phys. Lett.* **1996**, *256*, 454–464. [CrossRef]

79. Laurent, A.D.; Jacquemine, D. TD-DFT Benchmarks: A review. *Int. J. Quant. Chem.* **2013**, *113*, 2019–2039. [CrossRef]

80. Latouche, C.; Skouteris, D.; Palazzetti, F.; Barone, V. TD-DFT Benchmark on Inorganic Pt(II) and Ir(III) Complexes. *J. Chem. Theory Comput.* **2015**, *11*, 3281–3289. [CrossRef]

81. Martin, R.L. Natural Transition Orbitals. *J. Chem. Phys.* **2003**, *118*, 4775–4777. [CrossRef]